

Special Collection

Rapid Screening of Kinetic Models for Methane Total Oxidation using an Automated Gas Phase Catalytic Microreactor Platform

Solomon Gajere Bawa, Arun Pankajakshan, Conor Waldron, Enhong Cao, Federico Galvanin,* and Asterios Gavriilidis*^[a]

An automated flow micropacked bed catalytic reactor platform was developed to conduct pre-planned experiments for rapid screening of kinetic models. The microreactor was fabricated using photolithography and deep reactive ion etching of a silicon wafer, with a reaction channel width and depth of 2 mm and 420 μm respectively. It was packed with ca. 10 mg of 5 wt.% Pd/Al₂O₃ catalyst to perform methane combustion, which was the selected reaction to test the developed platform. The experimental system was monitored and controlled by

LabVIEW to which Python scripts for online design of experiments and data analysis were integrated. Within each experimental campaign, the platform automatically adjusted the experimental conditions, and the analysis of the product stream was conducted by online gas chromatography. The experimental platform demonstrated the capability of identifying the most probable kinetic models amidst potential models within two days.

Introduction

Automation and optimisation are advancing as promising extensions of microreactor technology^[1] and have the potential to save considerable time and effort in laboratory experimentation. Part of the challenge in an automated reaction set-up is the online determination of reactants and products concentration.^[2] The integration of analytical technology^[3] has made microreactors a powerful laboratory tool for reaction and kinetic studies.^[4] Some of the analytical tools used include UV-vis,^[5] infrared,^[6] Raman^[4a,7] spectroscopies, high-performance liquid chromatography (HPLC)^[8] and gas chromatography (GC).^[6d,9] Furthermore, microreactors used in flow have efficient mass and heat transfer characteristics required for isothermal kinetic studies.^[6c,d,10]

Automated systems have the ability to provide precise control of reaction conditions with minimal consumption of resources and user supervision.^[11] When combined with design of experiments (DoE) algorithms, they provide significant

advantages such as intelligent experimental design and highly informative experimental data for performing rapid kinetic studies. Automated systems could easily be adapted for reactions with similar protocol. Automated flow systems have been successfully applied for reaction discovery and screening,^[9a,12] as well as collecting data for model identification and parameter estimation of kinetic models,^[8b,d,13] focusing on liquid phase reactions. However, little effort has been devoted towards gas/solid reaction systems. In this work, such a reaction is investigated: methane total oxidation over Pd-based catalyst.

The process of obtaining a kinetic model requires significant time and resources, as large number of experiments are often needed. The major difficulties in obtaining a kinetic model are: i) obtaining a suitable model structure, i.e., set of reaction rate equations; and ii) obtaining statistically satisfactory estimates for the kinetic parameters, that can potentially be highly correlated^[14] and affected by structural^[15] or practical identifiability issues.^[16] Identification of the most appropriate kinetic model from a set of potential models involves first obtaining the model structure that predicts the system behaviour accurately and then estimating the parameters of the selected model precisely. Often, this identification task is challenging mainly due to two reasons. The first reason is the competing nature of potential models. Kinetic models of different reaction mechanisms may show a similar behaviour, leading to poor distinguishability and therefore it can be difficult to find the most appropriate model if experiments are poorly designed.^[17a] The second reason is the highly nonlinear structure of kinetic models, in which parameters can be correlated or poorly sensitive in the investigated range of experimental conditions.^[17b] This makes their unique estimation from the available measurements difficult.

Noble metals as well as transition metal oxides are utilised as methane combustion catalysts, with the former having

[a] S. G. Bawa, A. Pankajakshan, Dr. C. Waldron, Dr. E. Cao, Dr. F. Galvanin, Prof. A. Gavriilidis
 Department of Chemical Engineering
 University College London
 London, WC1E 7JE (UK)
 E-mail: f.galvanin@ucl.ac.uk
 a.gavriilidis@ucl.ac.uk

Supporting information for this article is available on the WWW under <https://doi.org/10.1002/cmtd.202200049>

This publication is part of a joint Special Collection of Chemistry—Methods and the European Journal of Organic Chemistry including contributions focusing on "Automating Synthesis: From Planning to Execution". Please visit chemistry-methods.org/collections to view all contributions.

© 2022 The Authors. Published by Wiley-VCH GmbH. This is an open access article under the terms of the Creative Commons Attribution License, which permits use, distribution and reproduction in any medium, provided the original work is properly cited.

higher activity. Methane combustion catalysts had been widely studied, with platinum and palladium standing out among the noble metals.^[18] The noble metals are usually dispersed on a support to improve the overall catalyst activity. Commonly used supports include silica,^[18–19] alumina,^[20] zirconia^[21] and ceria-zirconia.^[22] Palladium catalyst has been found to be more active than platinum for methane combustion but is associated with complex reaction mechanism due to the possible existence of more than one active phase,^[23] which are Pd and PdO,^[24] the latter being the most active phase.^[25] For Pd metal on alumina, oxidation of the metal begins at 200 °C and is complete at about 700 °C to produce PdO, which decomposes back to Pd metal at about 900 °C.^[25b]

Complete oxidation of methane is an interesting case study, because of the different mechanisms and kinetic models proposed in the literature. Researchers reported that the methane oxidation over Pd-based catalyst follows two distinct pathways on PdO and Pd dominated surfaces with different kinetics and proposed different mechanisms on Pd and PdO dominated states.^[26] A Mars–van Krevelen mechanism for complete oxidation of methane has been reported,^[20b,21c,27] which involves a redox reaction of the catalytic site. Other researchers found Langmuir–Hinshelwood kinetic models as plausible.^[28] Eley–Rideal mechanism has been reported to account for catalytic oxidation of methane,^[29] while empirical power laws have also been proposed.^[20c,30]

The aim of this paper is to develop an integrated experimental/computational platform for gas phase catalytic reactions that could conduct automated experiments to rapidly screen potential kinetic models. The platform is demonstrated for the complete methane oxidation on palladium catalyst. It allows the online identification of candidate kinetic models by performing online kinetic parameter estimation and leveraging model discrimination techniques for optimal kinetic model selection. Probability criteria for model selection based on hypothesis testing are employed to aid the kinetic model screening process. A parameter estimability analysis is carried out on selected kinetic models to identify issues and limitations on proposed model structures.

Results and Discussion

Temperature distribution in the micropacked bed

The axial temperature profile along the catalyst bed, which occupied the reaction channel, was studied in the range of set temperatures 150–400 °C (see Figure 1). We observed a variation within ± 3 °C at the maximum investigated temperature of 400 °C. Thus, the microreactor was considered to be isothermal.

Reproducibility of experiments in the automated platform

Prior to investigating the platform reproducibility, catalyst stability was established by running a 200 min experiment at 300 °C (see Supporting Information, Figure S2). Furthermore,

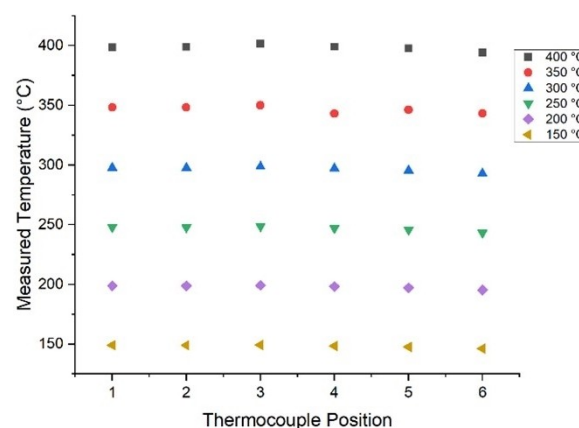


Figure 1. Temperature distribution along the catalyst bed in the packed bed microreactor at the set temperatures indicated. Experimental conditions: 11.4 mg of 5% Pd/Al₂O₃, 53–63 μ m catalyst particles, 10 mL/min total inlet flowrate, 1.5% CH₄, 3% O₂, 30% He, 65.5% N₂.

the carbon balance during methane oxidation closed within ± 2.5 % (see Supporting Information, Figure S3). A blank experiment (empty microreactor) was conducted at the upper limit of the temperature range (350 °C) and showed no homogeneous reactions. The fractional factorial design of experiments, consisting of eight experiments, was used to ascertain the reproducibility of the developed platform. Four replicate campaigns were executed using two different reactors (of the same dimensions and containing the same amount of catalyst, 11.4 mg). In campaigns 1 and 2, experiments were performed on different days, but with the same reactor, while in campaigns 3 and 4, a different microreactor was used, and the experiments were conducted on different days. Good reproducibility was observed, as shown in Figure 2 from the experimental results in

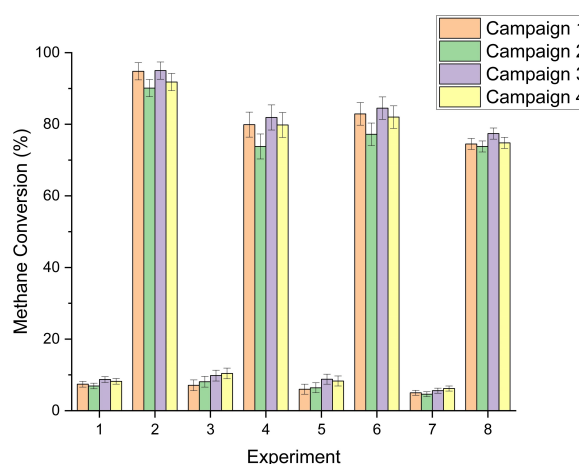


Figure 2. Replicates of fractional factorial experiments results of methane combustion on 11.4 mg of 5% Pd/Al₂O₃, 63–75 μ m catalyst performed in the automated platform. Campaigns 1 and 2, were performed with the same microreactor, while campaigns 3 and 4, were performed with a different microreactor. The error bars represent one standard deviation (%) and the experimental conditions are provided in Supporting Information, Table S1. Both microreactors had dimensions as given in microreactor assembly and catalyst loading sub-section of the experimental and theoretical section.

terms of methane conversion, (for details see Supporting Information, section 9.1).

During the fractional factorial experiments, good agreement between the set temperature and the measured (process) reactor temperature was observed (see Supporting Information, Figure S4). The actual and set profiles showed the same rate of heating and cooling. As such, natural convection was deemed adequate for heat removal from the microreactor. The average pressure in the packed bed was calculated through an empirical pressure drop model, which was based on the Ergun equation and contained also a correction factor, so that the predicted reactor inlet pressure matched the measured one (see Supporting Information, section 8).

Estimation of measurement error

The pooled standard deviation of methane, oxygen and carbon dioxide mole fractions, which were the response variables for the methane combustion over Pd/Al₂O₃, were computed based on the method outlined in the software framework for screening of kinetic models sub-section of the experimental and theoretical section using experimental data from factorial design of experiments. The pooled standard deviations were estimated using Equation (2) and found to be 0.00043, 0.00202 and 0.0005 in mole fraction for methane, oxygen and carbon dioxide respectively. The measurement error variance calculated from Equation (2) was used to estimate the parameter variances, thus accounting for uncertainties associated to measurements obtained from the automated system.

Model adequacy and probability of correctness

Kinetic model adequacy test was performed using the probability criteria described in the model adequacy and probability of correctness sub-section of the experimental and theoretical section using the experimental data obtained from Latin hypercube sampling (LHS) (see Supporting Information, section 9). The performance of all the examined kinetic models is presented in Table 1. When $\chi_{ref}^2/\chi^2 > 1$, the model can be

considered adequate. As observed, the most probable models were Mars–van Krevelen (slow product desorption, Model 12) and two Langmuir–Hinshelwood models (dissociatively adsorbed oxygen, Model 9 and adsorbed molecular oxygen, Model 8). Models 12, 9 and 8 had probability of model correctness of 49%, 40% and 11% respectively (see Table 1); these were selected, while the other models had 0% probabilities and were rejected. The selected models, which are in accordance with Langmuir–Hinshelwood and Mars–van Krevelen mechanisms have been reported for methane combustion over palladium-based catalyst in the literature. Specchia *et al.*^[31] after considering kinetic models based of Eley–Rideal, Langmuir–Hinshelwood and Mars–van Krevelen, rejected the Eley–Rideal models for lack of fit to the obtained experimental data, which is similar to our work. Model 8, which is Langmuir–Hinshelwood kinetic model with molecular adsorbed oxygen is not often used in literature for methane combustion over palladium-based catalyst. Models 9 and 12 were among the seven selected models reported by Hurtado *et al.*,^[27a] who concluded that Mars–van Krevelen mechanism with slow desorption of products, Model 12 was the best model, after considering twenty-one kinetic models.

Practical identifiability analysis of kinetic model parameters

Confidence intervals and Student's *t*-test are used to ascertain the statistical precision of kinetic model parameter estimates. A lower computed *t*-value as compared to reference is indicative of a poor estimated parameter. All three most promising models selected after parameter estimation (Models 8, 9 & 12) contain six kinetic parameters. Parameter estimation results in terms of estimated value and a-posteriori statistics (95% confidence intervals and *t*-test results) for these models are reported in Table 2. Kinetic parameters of Model 8 (Table 2) were not all estimated satisfactorily based on the *t*-statistics, since only four out of the six parameters were precisely estimated, and were associated with low confidence interval. Similar trend was observed with Model 9, with five out of the six kinetic parameters estimated with good precision as shown in Table 2. Both models 8 & 9 considered surface reaction as the rate limiting step. For Model 12, three out of the six parameters were estimated satisfactorily (Table 2). The parameter which is associated with the pre-exponential factor of the catalyst surface oxidation step (θ_1) and the parameter related to activation energy for catalyst surface oxidation (θ_2) of Model 12 were poorly estimated. The values for activation energies and heats of adsorption were computed using Equations (15) and (16) from the obtained values in Table 2. The activation energies for Model 8 & 9 were 74.9 and 79.3 kJ/mol respectively, which were in agreement with a reported value of 76.3 kJ/mol.^[27a] The heats of adsorption of oxygen and methane for Model 8, were 39.5 and 13.5 kJ/mol, which were close to the reported values of 37.0 and 10.4 kJ/mol respectively but were associated with high uncertainty as seen from their confidence interval values (Table 2); as such they were poorly estimated. For Model 9, the heats of adsorption for both oxygen and methane were 96.3

Table 1. Results of model adequacy test and probability of model correctness for the kinetic models of catalytic methane combustion shown in Table 5.

Model	χ^2	χ_{ref}^2	χ_{ref}^2/χ^2	Probability [%]
1	279	107	0.369	0
2	248	107	0.431	0
3	270	107	0.396	0
4	256	107	0.418	0
5	275	105	0.381	0
6	272	105	0.386	0
7	676	105	0.155	0
8	<u>205</u>	<u>103</u>	<u>0.502</u>	<u>11</u>
9	<u>200</u>	<u>103</u>	<u>0.515</u>	<u>40</u>
10	257	103	0.401	0
11	279	105	0.376	0
12	<u>199</u>	<u>103</u>	<u>0.518</u>	<u>49</u>
13	279	103	0.369	0

Parameter	Estimate	Confidence interval [\pm]	t-value	Reference t-value
Model 8				
θ_1	9.16	0.20	45.18	1.66
θ_2	7.49	2.16	3.46	
θ_3	3.89	0.40	9.64	
θ_4	3.95	3.35	1.18^[a]	
θ_5	4.45	0.60	7.44	
θ_6	1.35	6.14	0.22^[a]	
Model 9				
θ_1	9.08	0.23	39.86	1.66
θ_2	7.93	2.10	3.77	
θ_3	4.49	0.95	4.71	
θ_4	9.63	4.67	2.06	
θ_5	4.22	0.58	7.30	
θ_6	1.66	5.19	0.32^[a]	
Model 12				
θ_1	3.52	2.23	1.58^[a]	1.66
θ_2	12.14	17.77	0.68^[a]	
θ_3	6.25	0.32	19.69	
θ_4	7.81	6.31	1.06^[a]	
θ_5	10.46	0.21	48.41	
θ_6	8.88	1.87	4.21	

[a] t-values below the threshold value

and 16.6 kJ/mol respectively, which were not far from reported values of 104.2 and 21.5 kJ/mol respectively^[31] but the heat of methane adsorption estimate was associated with high level of uncertainty from the observed confidence interval (Table 2). Weaver *et al.*^[32] reported an estimated value of 16.2 kJ/mol, as binding energy for methane adsorption on PdO by applying density functional theory calculation. The values obtained for the activation energies for oxidation and reduction of catalyst surface with regards to Model 12, were 121.4 and 78.0 kJ/mol which were above reported values of 51.5 and 16.8 kJ/mol respectively.^[27a] However, these values were not precisely estimated. The enthalpy of desorption of 89.8 kJ/mol (obtained from θ_6), which was precisely estimated, was not far off the reported value of 108.5 kJ/mol.^[27a]

Since not all parameters were precisely estimated, it is important to check the practical identifiability of parameters of the selected models. The Fisher information Matrix (FIM) is the easiest way to check practical identifiability after parameter estimation. If the FIM is fully ranked and not singular, the model parameters are identifiable. As shown in Table 3, all three selected kinetic models are fully ranked which indicates that all the kinetic parameters are practically identifiable.

Table 3. Results of practical identifiability test of the kinetic models of catalytic methane combustion appearing in Table 5.

Model	Model category	Rank	Remark
8	Langmuir–Hinshelwood	6/6	FIM fully ranked
9	Langmuir–Hinshelwood	6/6	FIM fully ranked
12	Mars–van Krevelen	6/6	FIM fully ranked

Furthermore, the Relative Fisher Information index (RFI)^[17b] of experiments was quantified from the trace of FIM for the selected models in the LHS-sampled design space of experimental conditions. As observed in Figures 3–5 for all the models, about one-third of the experimental conditions (points marked in red) are characterised by a low information content. The numbers on top of each point in the design space are the ratio of oxygen to methane in the feed. The region that is associated with low amount of information content is within the low total flowrate portion of the design space. Almost all the experiments within this design space were not useful for the identification of kinetic model parameters. Comparing the RFI of the three models in Figure 6, only about two-thirds of the experiments were highly informative, and information about the selected models slightly varies with the experimental conditions within the design space, (details on experimental conditions are in Supporting Information, Table S2). Hence, to optimally design experiments to improve the practical identifiability of the poorly estimated parameters one should exploit

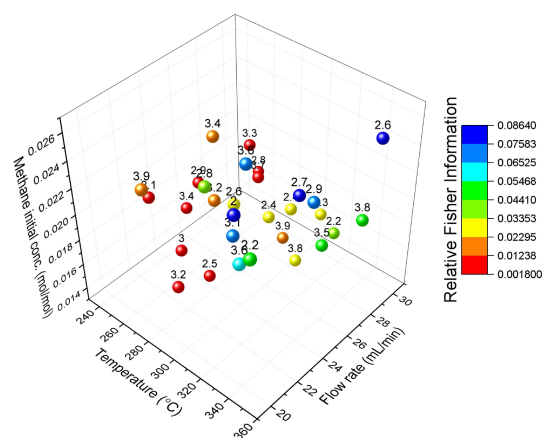


Figure 3. Mapping of the Relative Fisher Information index in the design space for Model 8 from Latin hypercube sampling experimental data. The number above each point is the oxygen to methane mole ratio.

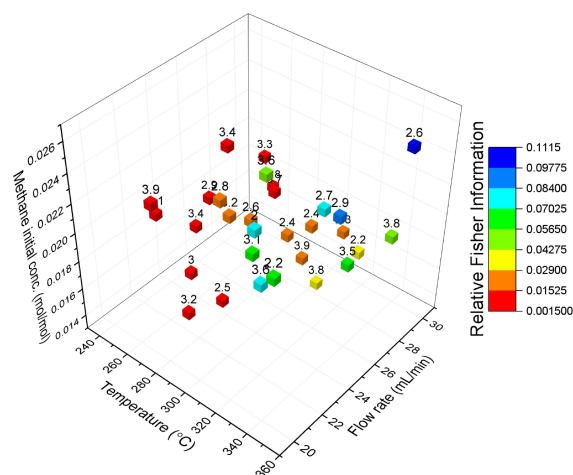


Figure 4. Mapping of the Relative Fisher Information index in the design space for Model 9 from Latin hypercube sampling experimental data. The number above each point is the oxygen to methane mole ratio.

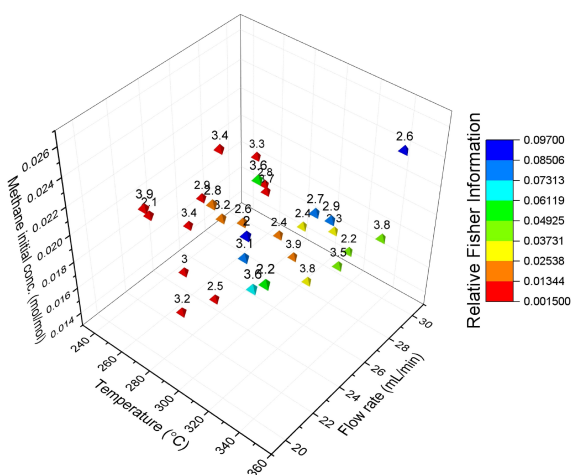


Figure 5. Mapping of the Relative Fisher Information index in the design space for Model 12 from Latin hypercube sampling experimental data. The number above each point is the oxygen to methane mole ratio.

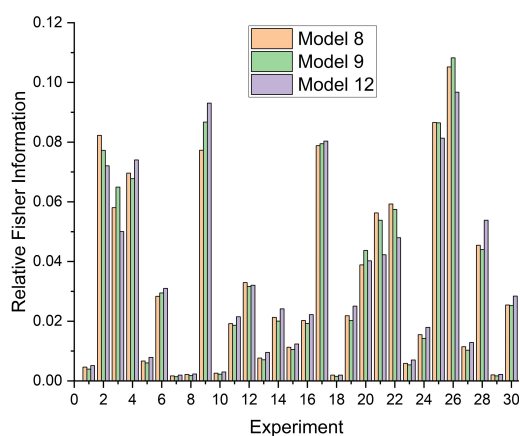


Figure 6. Ranking of Latin hypercube sampling experiments based on the Relative Fisher Information index.

the experimental regions associated with high information, since it has been established that the parameters are identifiable. The experimental conditions which were associated with the highest amount of information are those at high temperature and high initial concentration of methane and can be used to initialise model-based design of experiments (MBD_{oE}) methods for improving practical identifiability of model parameters; however, this was outside the scope of this paper.

The LHS-generated experimental data were used to compare with the predicted data of models 8, 9 & 12 (the selected models according to statistical analysis). A good agreement of model prediction with experimental data of all measured mole fractions was established for the three models, as shown in Figures 7a,b,c as minimal deviations of measurements from model predictions were observed. In order to visualise the difference in the performance of the models, the predictions of the models against the experimental data were analysed for each measured species. Considering measurements of concentrations against predictions of the selected models, as shown in Figure 8, a similar pattern was observed, but differences existed

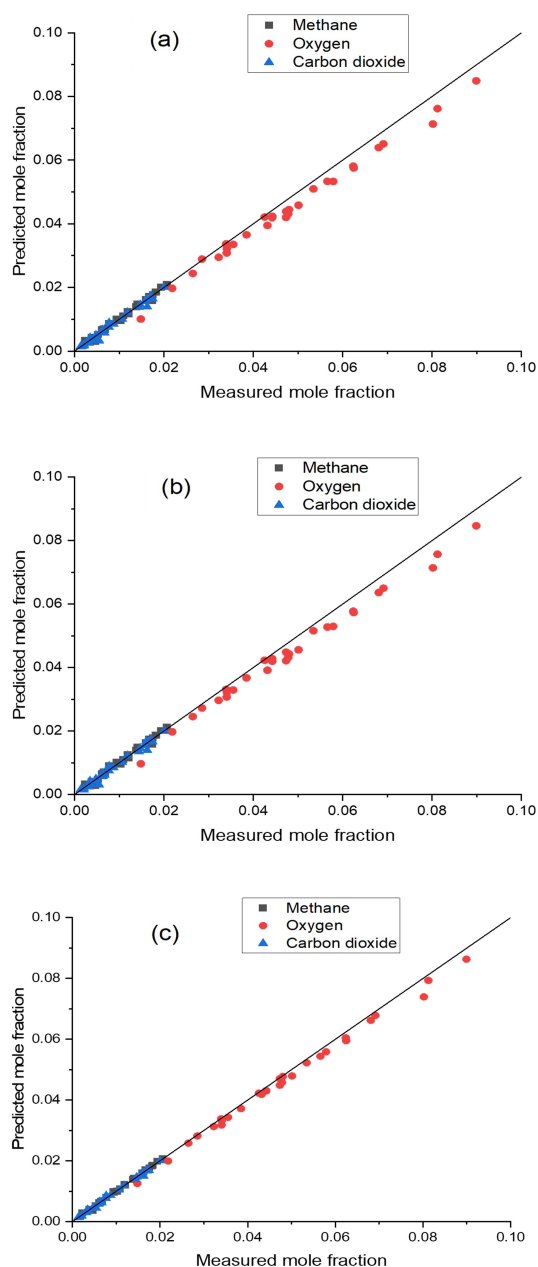


Figure 7. Parity plots for reactor outlet mole fractions based on (a) Langmuir–Hinshelwood rate expression (Model 8), (b) Langmuir–Hinshelwood rate expression (Model 9), (c) Mars–van Krevelen rate expression (Model 12) of methane combustion from Latin hypercube sampling experimental data.

among the three models. Model 12 has lower deviation from the diagonal line, which is more evident for the parity plots of methane (Figure 8a) and oxygen (Figure 8b). To further visualise the differences in terms of model performance, residual plots, which is the difference between predicted and experimental data, are shown in Figures 8 d–f. From the plots, Model 12 had the lowest residual values for all the species, which agrees with the probability of model correctness (see Table 1) of this model having the highest value of 49%. Few outliers were observed from the data, which were outside the region of two-standard deviation limits. A robust experimental design approach, such

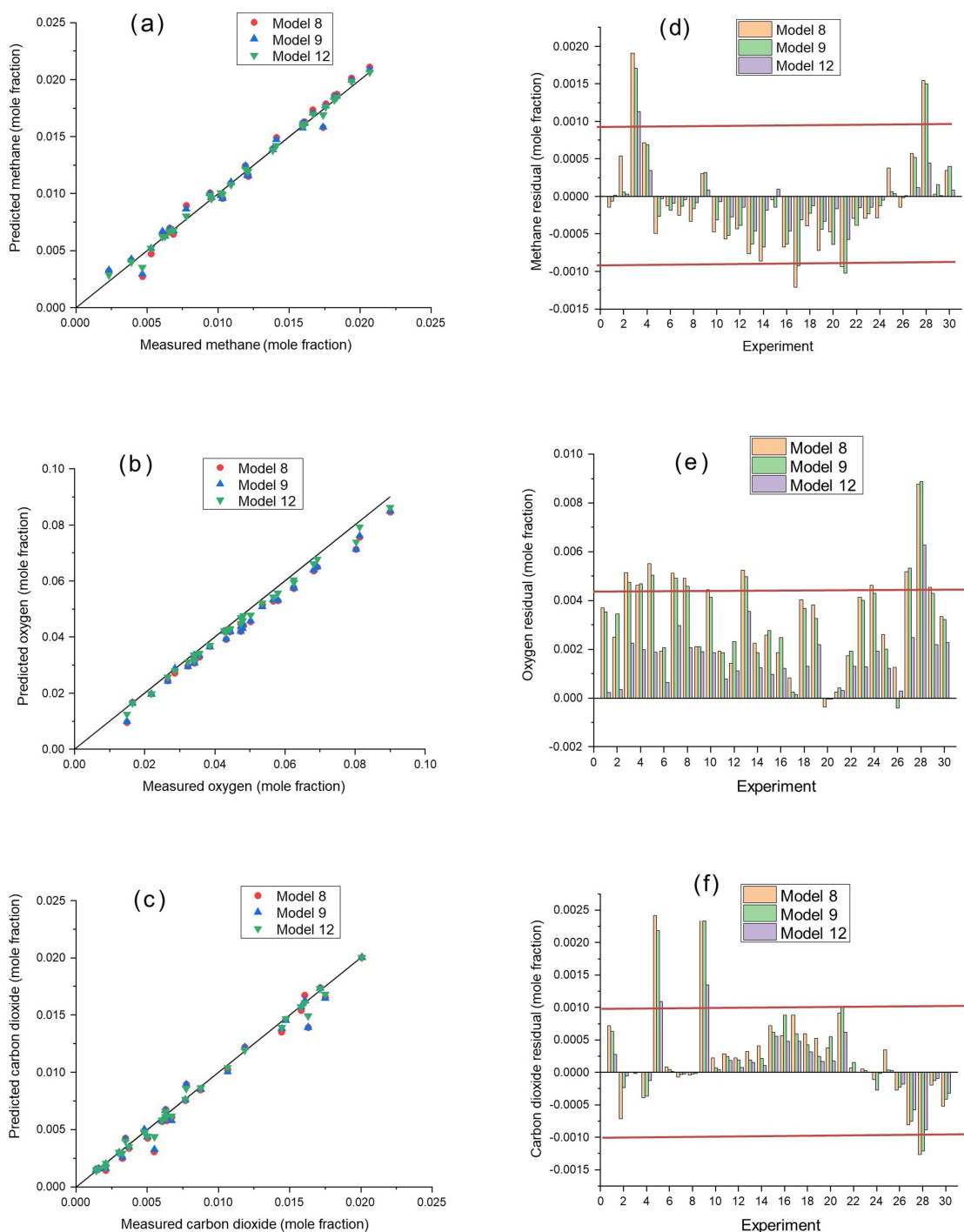


Figure 8. Reactor outlet mole fractions parity plots of the selected models for (a) methane, (b) oxygen, (c) carbon dioxide and residual plots of the selected models for (d) methane, (e) oxygen (f) carbon dioxide, using the Latin hypercube sampling experimental data. The red lines represent the two-standard deviations limits.

as MBD_{oE} for model discrimination, will be vital in distinguishing between these competing models.

Conclusion

The experimental platform developed, demonstrated the capability of conducting automated experiments based on user-defined conditions using factorial and Latin hypercube sampling experimental designs. The automated platform successfully executed a large number of experiments, demonstrating

its capability for rapid screening of kinetic models within a short time. The robustness of the platform was established, as it could handle large number of experiments without user attention in a safe manner and screen proposed kinetic models within 48 h. The platform showed consistency in terms of control of input variables, such as reactant flow rate, reaction temperature and pressure measurement, as well as good reproducibility of results, as evident by a set of repeated factorial experiments. Similar level of agreement between prediction and experiments was observed between Langmuir-Hinshelwood (dissociatively and molecular adsorbed oxygen) and Mars–van Krevelen (slow product desorption) kinetic models, which were the most probable models from the ones investigated, both showing a good fitting performance, within the range of controlled variables studied, as demonstrated by the obtained parity plots. As such, these models could serve as useful tool for the prediction of reaction behaviour within the experimental design space considered. Some of the kinetic parameters of the models were not precisely estimated. However, the estimated kinetic parameters can be used as prior information for a more intelligent experimental design, such as model-based design of experiments. Work on the application of model-based design of experiments, which is a more sophisticated method for distinguishing the competing models and estimating of kinetic parameters with the highest precision is in progress.

Experimental and Theoretical Section

Microreactor assembly and catalyst loading

The silicon-glass microreactor employed in this work is shown in Figure 9a. It was fabricated using photolithography and deep reactive ion etching (DRIE) process. Anodic bonding at 400 °C and 500 V was used for sealing the structured silicon wafer to a glass cover. The reaction channel was 2 mm wide and 420 μm deep. The microreactor had six dead-end slots perpendicular to the reaction channel for inserting thermocouples to monitor the temperature along the catalyst bed. A catalyst retainer at the end of the reaction

channel held the catalyst in place. The microreactor assembly (see Figure 9b) included parts for heating, connecting the reaction gases and analysis section and holding the microreactor in place. The heating chuck was an integral part of the microreactor assembly and consisted of a heating block (54 mm × 40 mm × 2.5 mm), ceramic heater (ULTRAMIC, Watlow), (at the top right of Figure 9b, its electric wire connection is shown) and reactor clamp (54 mm × 40 mm × 2.5 mm). The heating block kept the ceramic heater in place. The microreactor was placed between the reactor bottom (35 mm × 16 mm × 10 mm) and top (35 mm × 16 mm × 5 mm) feedthrough connectors. The bottom connector was at the same level with the heating block and contained grooves for high temperature O-rings (Perlast G80 A, O Rings Ltd) for sealing the inlet/outlet of the microreactor. The reactor clamp held the microreactor in firm position on the ceramic heater for effective and uniform heating. The catalyst, 5% Pd/Al₂O₃ (Johnson Matthey) in powder form, was pelletised and then crushed to obtain the required size range (53–63, 63–75 & 75–90 μm) fractions by sieving. For loading the catalyst, the microreactor was mounted in a Perspex feedthrough assembly and connected to a vacuum line via its outlet port. Using a 200 μl pipette tip as funnel, 10 mg of catalyst was weighed and loaded into the reactor through the inlet port of the microreactor. The temperature profile along the catalyst bed was obtained with six thermocouples (K-type, Omega Engineering) positioned inside the six slots perpendicular to the reaction channel.

Experimental platform

The feed stream to the microreactor consisted of methane, oxygen, helium and nitrogen delivered using mass flow controllers (Brooks, 5850TR). Oxygen and methane (5% CH₄/He) were mixed at a junction, while nitrogen served as an internal standard. Pressure sensors (Honeywell, 40PC, 100 psig) were connected at the inlet and outlet tubing (Polytetrafluoroethylene (PTFE), VICI Jour) of the reactor assembly for pressure monitoring. A pressure controller (Brooks, 5866) was positioned after the microreactor to maintain the desired outlet pressure. The analysis of feed and effluent streams was performed using an online gas chromatograph (Agilent, 7890A). The configuration of the gas chromatograph included a pneumatic sampling valve, sampling loop of 0.25 mL, GS-Carbon PLOT (Agilent) and HP-PLOT molecular sieve (Agilent) columns for separating CO₂ and permanent gases respectively, and thermal conductivity detector (TCD). OpenLab CDS 2.4 GC software

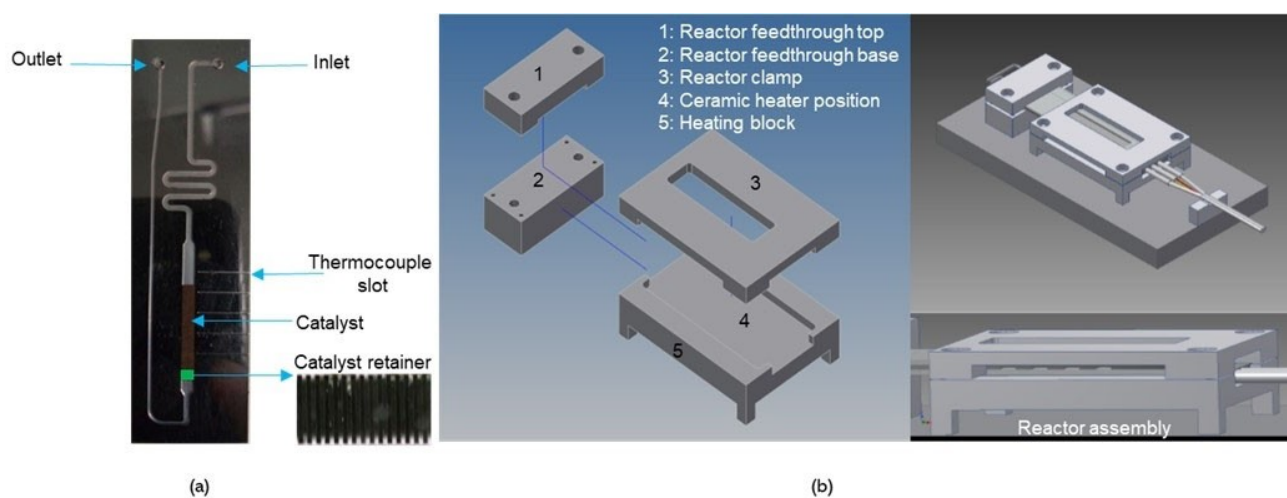


Figure 9. (a) Silicon-glass microreactor packed with Pd/Al₂O₃ catalyst, (b) Microreactor assembly for heating and interfacing the microreactor with inlet/outlet streams.

was used for method development and data processing during the analysis. Figure 10 shows the major components of the set-up, which included reactant delivery section, microreactor, online analysis with GC and the control system, which contained the

Python algorithms, integrated to LabVIEW code for automating the entire experimental process.

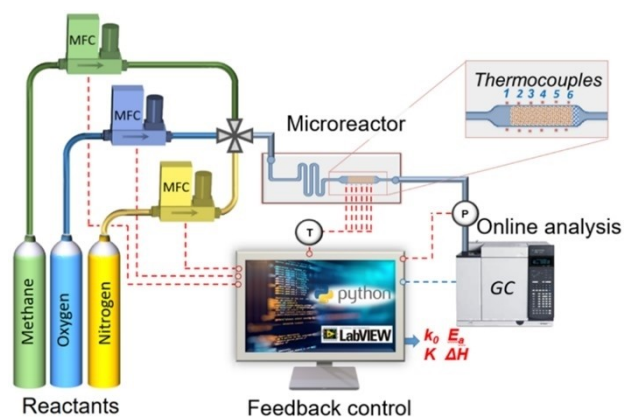


Figure 10. Automated experimental set up for methane oxidation reaction in a packed bed microreactor. MFC: mass flow controller, P: pressure controller, T: temperature controller, GC: gas chromatograph.

Experimental platform user interface for automation and control

Laboratory Virtual Instrument Engineering Workbench (LabVIEW) environment was used for automating the experimental process. The LabVIEW code developed in this work allowed the user to run a list of pre-planned experiments. The automation process in LabVIEW consisted of four loop elements (see Figure 11) namely *Timed loop*, *Flat sequence*, *Case structure*, and *While loop*. The *Timed loop* repeated a given set of commands at given frequency within the specified experimental duration. It controlled the execution cycle, which checked and compared the set values to process values within a stipulated period for each experiment. To move out of the *Timed loop* one of two given conditions should be satisfied. The two conditions were exceeding the experimental duration or the imposed safety limits. Temperature and pressure safety limits were set to 400 °C and 3 barg respectively, to ensure the safe execution of the experiments. The user had the liberty to set the cycle time (frequency) in the *Timed loop*; in this work, each loop cycle took 10 s for execution, which translates to 120 cycles for an experimental duration of 20 min. A sequential series of events was executed one after the other by using a *Flat sequence*

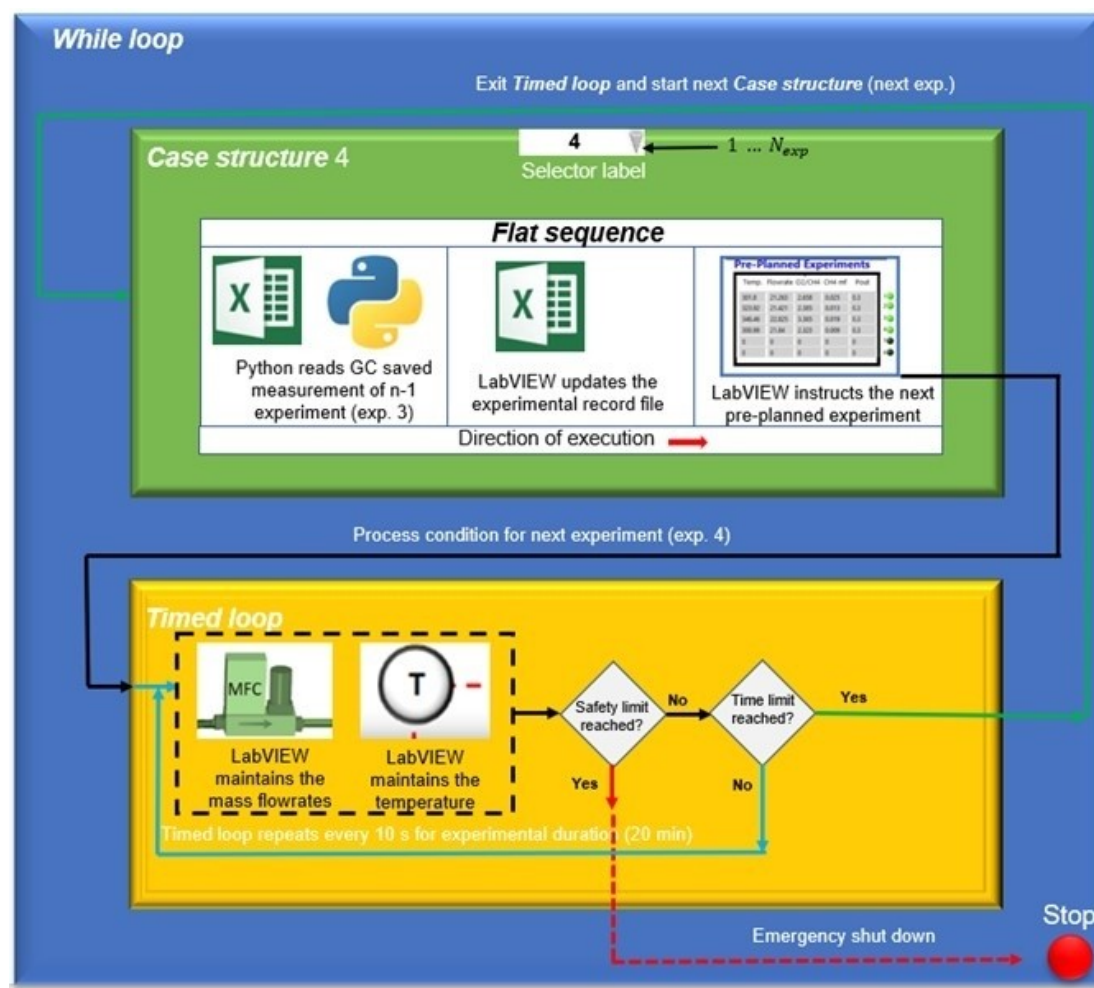


Figure 11. Experimental platform user interface implemented for automation, showing the four loop elements, which include *While loop*, *Case structure*, *Timed-loop* and *Flat sequence*.

structure. The *Flat sequence structure* was made up of frames, which were executed in an orderly sequence. From the second to the n -pre-planned experiment, the Python code accessed the saved GC results, as the first set of command in the *Flat sequence*. Next, the record file was updated with the experimental conditions and the outlet stream composition in an Excel file. Finally, the last command in the *Flat sequence* sent the next pre-planned experimental conditions to the hardware via the *Timed loop*. The *Case structure* contained multiple subdiagrams, which were set of commands within the *Case structure* executed for each experiment. For eight pre-planned experiments, there were eight subdiagrams within the *Case structure* and the ninth *case structure* was added as the default setting. The number of pre-planned experiments was set at the selector label using a numerical subdiagram identifier. The selector label at the top line border of the *Case structure* displayed the value of the subdiagram to be executed. The *Case structure* controlled the sequence of experimental runs in an ascending order. All the previous loops and structure stated were within the *While loop* which controlled the repetitive operation in a virtual instrument (VI), until all the planned experiments were performed. After that the platform would be at the default settings specified at the commencement of the experiment, which were set at temperature of 20 °C and zero for the flowrate of reactants. The automated process came to an end when the *While loop* was exited. This happened either when the stop button was activated in the LabVIEW front panel or the iteration number in the *While loop* (LabVIEW block diagram) became equal to the number of the *case structure* default setting as specified.

Software framework for screening of kinetic models

The software framework used for screening of kinetic models consisted of a stand-alone Python module which was integrated to the microreactor unit using the Python-LabVIEW interface described above. The framework contained a set of Python functions for i) Design of experiments, ii) Calibration of experimental platform by estimating the random error in observations, iii) Parameter estimation, iv) Screening of kinetic models and v) Practical identifiability study and information mapping of adequate models. The flowchart of the framework is illustrated in Figure 12.

Before describing the steps in the framework, it is important to know the need for each of them, which is explained using a general kinetic model represented by a set of differential and algebraic equations (DAEs) in the form

$$\begin{aligned} \dot{\mathbf{x}} &= \mathbf{f}(\dot{\mathbf{x}}, \mathbf{x}, \mathbf{u}, \boldsymbol{\theta}) = 0 \\ \hat{\mathbf{y}} &= \mathbf{g}(\mathbf{x}, \mathbf{u}, \boldsymbol{\theta}) \end{aligned} \quad (1)$$

In Equation (1), $\mathbf{x} \in \mathbb{R}^{N_x}$ is the vector of differential state variables (mole fractions of methane, oxygen, carbon dioxide and water), $\mathbf{u} \in \mathbb{R}^{N_u}$ is the vector of input controls or conditions of experiments (reaction temperature, inlet methane mole fraction, oxygen to methane mole ratio and total flowrate of reactants), $\boldsymbol{\theta} \in \mathbb{R}^{N_\theta}$ is the vector of unknown model parameters (pre-exponential factor, activation energy and enthalpy of adsorption), $\hat{\mathbf{y}} \in \mathbb{R}^{N_y}$ is the vector of model predictions for the response variables \mathbf{y} , which are the measured variables at the reactor outlet (mole fractions of methane, oxygen and carbon dioxide). In the study of chemical kinetics with a goal of obtaining predictive kinetic models, it is important to identify and minimise the sources of uncertainties in model predictions. The three major sources of uncertainties in model predictions $\hat{\mathbf{y}}$ can be categorised as: (i) errors in the measurements $\delta\mathbf{y}$, (ii) errors in the input controls $\delta\mathbf{u}$ and (iii) errors

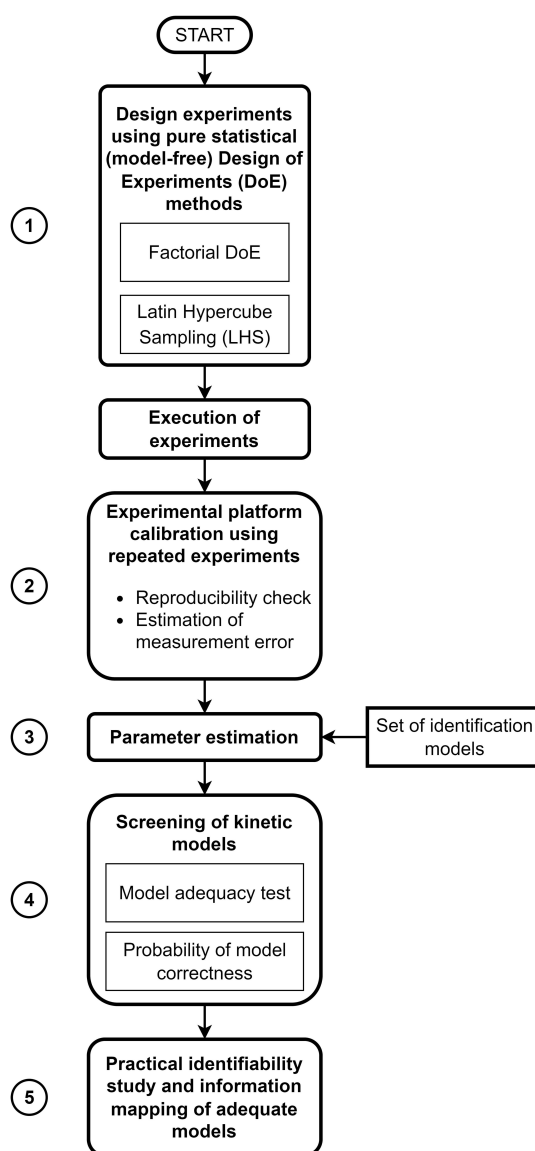


Figure 12. Block diagram showing the workflow of the software framework used for screening of kinetic models.

in parameter estimates $\delta\boldsymbol{\theta}$. Among these errors, except the error in parameter estimates that is estimated, the other two are solely related to the experimental platform and are directly controllable. Therefore, it is important to assure that the platform is set to a level of minimum $\delta\mathbf{y}$ and $\delta\mathbf{u}$ with a reliable estimate of both errors. Although cases exist in which errors in both input controls and response variables, that is, $\delta\mathbf{u}$ and $\delta\mathbf{y}$ are considered in estimating unknown and non-measurable model parameters^[33], we focus on the case where there are errors in the measured response variables only, which should also be evaluated in the calibration step. In the framework shown in Figure 12, we estimate the random measurement error $\delta\mathbf{y}$ in step 2 from the experiments designed in step 1. The random measurement error is used along with the data in the estimation of the unknown model parameters in step 3. In step 4, we use the results of step 3 to select the most appropriate models based on an adequacy test and a probability of model correctness criterion. In step 5, we study the uncertainty in parameter estimates $\delta\boldsymbol{\theta}$ and its allocation over the design space for the selected models from step 4.

Design of experiments (DoE) methods

Design of experiments methods are pure statistical sampling techniques which are used to sample the input design space, such that the variability within the input domain is captured fully to bring out the essential features of interest. The experiments designed using the DoE methods are also used for the purpose of estimation of random error in the observations (from few repetitions of the DoE experiments). In this work, two DoE methods were used – i) Fractional factorial design and ii) Latin hypercube Sampling (LHS). The experiments designed using fractional factorial design contain all possible combinations of high and low values of the input design variables, thus covering the variability across the full input domain including the interactions between input variables. The experiments designed using the LHS method, on the other hand, allow studying the variability of output variables due to small changes in an input variable inside its domain.

Estimation of measurement error

Suppose a campaign of N factorial experiments are repeated m times. In each factorial experiment, N_y number of response variables are measured at a steady state time. This will generate N different samples, each of size $m \times N_y$. Each of the N_y dimensional observations in any of the N samples is assumed to be corrupted with uncorrelated normally distributed measurement error with zero mean vector and N_y dimensional diagonal covariance matrix Σ_y , which is to be estimated using this step. The method of pooled standard deviation^[34] was used to define the standard deviation of the measurement error of each of the response variables and these were determined as the square root of the pooled variance, computed for each response variable as

$$s_{p_j}^2 = \frac{\sum_{i=1}^N (n_i - 1) s_{ij}^2}{\sum_{i=1}^N (n_i - 1)} \quad \forall j = 1, \dots, N_y \quad (2)$$

In Equation (2), $s_{p_j}^2$ is the pooled variance of the j -th response variable, n_i is the size of i -th sample, which in this case is m , because all experiments are repeated m times and s_{ij}^2 is the variance of j -th response variable in the i -th sample, which is computed as

$$s_{ij}^2 = \frac{1}{n_i - 1} \sum_{k=1}^{n_i} (y_{kj} - \bar{y}_{ij})^2 \quad \forall i = 1, \dots, N; \quad \forall j = 1, \dots, N_y \quad (3)$$

In Equation (3), \bar{y}_{ij} is the mean of the j -th response variable in the i -th sample.

Parameter estimation

In the parameter estimation step, the dataset \mathbf{Y} with an estimate of the random measurement error is fitted to the different identification models by minimising some function of the residuals (the difference between experimental values and model predictions). Additional experiments other than those used for the calibration purpose may be performed before the parameter estimation step. In this work, parameter estimation was carried out using the maximum-likelihood method within the Frequentist approach^[35]. The likelihood function $L(\boldsymbol{\theta}, \mathbf{Y})$ provides the likelihood of observing the dataset \mathbf{Y} given the model parameters $\boldsymbol{\theta}$. For the numerical stability of the optimisation algorithm, parameter estimation was solved by minimising the negative log-likelihood function according to Equation (4).

$$\begin{aligned} & \underset{\boldsymbol{\theta} \in \Theta}{\text{minimize}} \quad -\ln L(\boldsymbol{\theta}, \mathbf{Y}) \\ & = \frac{N_E \cdot N_y}{2} \ln(2\pi) + \frac{N_E}{2} \ln(\det|\Sigma_y|) \\ & \quad + \frac{1}{2} \sum_{i=1}^{N_E} [\mathbf{y}_i - \hat{\mathbf{y}}_i(\boldsymbol{\theta})]^T \Sigma_y^{-1} [\mathbf{y}_i - \hat{\mathbf{y}}_i(\boldsymbol{\theta})] \end{aligned} \quad (4)$$

In Equation (4) $\mathbf{y}_i - \hat{\mathbf{y}}_i(\boldsymbol{\theta})$ is the $N_y \times 1$ dimensional vector of residuals in i -th experiment, N_E is the total number of experiments conducted and Σ_y is the $N_y \times N_y$ measurement covariance matrix, which is a diagonal matrix with pooled variances of response variables along the diagonal calculated from Equation (2).

Model adequacy and probability of correctness

After the parameter estimation step, the fitting quality, or the adequacy of kinetic models at the maximum likelihood parameter estimate $\hat{\boldsymbol{\theta}}$ is evaluated using the χ^2 goodness of fit test (Equation (5)). The test compares the computed sum of squared standard residuals at the maximum likelihood parameter estimate to the χ^2 value from the χ^2 distribution with $N_E \cdot N_y - N_\theta$ degrees of freedom and α significance level (reference value χ_{ref}^2). A smaller value of computed χ^2 compared to the reference value indicates an adequate fit of the model to the observed data.

$$\chi^2 = \sum_{i=1}^{N_E} [\mathbf{y}_i - \hat{\mathbf{y}}_i(\hat{\boldsymbol{\theta}})]^T \Sigma_y^{-1} [\mathbf{y}_i - \hat{\mathbf{y}}_i(\hat{\boldsymbol{\theta}})] \quad (5)$$

The result of adequacy test is used to define a probability criterion which is used for the rapid screening of kinetic models in the automated flow reactor platform. According to the proposed probability criterion, the probability not to reject model s , Pr_s is defined as

$$\text{Pr}_s = \frac{\Pr(\chi_s^2 < \chi_{N_E \cdot N_y - N_\theta}^2(1 - \alpha))}{\sum_{s=1}^{N_m} \Pr(\chi_s^2 < \chi_{N_E \cdot N_y - N_\theta}^2(1 - \alpha))} \cdot 100\% \quad \forall s = 1, \dots, N_m \quad (6)$$

In Equation (6), the probability value $\Pr(\cdot)$ in the numerator and denominator corresponds to the p -value obtained in the χ^2 goodness of fit test for the s -th model. The probability calculated from Equation (6) is used as probability of model correctness in the kinetic model screening procedure. Models which have the highest probabilities Pr_s are deemed the most adequate to represent the system.

Practical identifiability study and information mapping

The uncertainty in estimation of parameters of the most probable models selected from the previous model screening step is evaluated using a practical identifiability study described as follows. The identifiability of model parameters can be quantified locally, that is, at the maximum likelihood estimate by the observed Fisher Information Matrix (FIM) $\mathbf{H}(\hat{\boldsymbol{\theta}})$ which is approximated as

$$\mathbf{H}(\hat{\boldsymbol{\theta}}) = \sum_{i=1}^{N_E} \left(\frac{d\mathbf{y}}{d\boldsymbol{\theta}} \right)_i^T \Sigma_y^{-1} \left(\frac{d\mathbf{y}}{d\boldsymbol{\theta}} \right)_i \Big|_{\boldsymbol{\theta}=\hat{\boldsymbol{\theta}}} \quad (7)$$

In Equation (7), $\mathbf{H}(\hat{\boldsymbol{\theta}})$ denotes the Fisher information matrix computed after N_E experiments and $\frac{d\mathbf{y}}{d\boldsymbol{\theta}}$ represents the $N_y \times N_\theta$ dimensional sensitivity matrix. The parameter covariance matrix \mathbf{V}_θ , which is the common measure of precision of parameter estimates, is approximated as the inverse of FIM.

$$\mathbf{V}_\theta = \left\{ [\mathbf{V}_\theta^0]^{-1} + \sum_{i=1}^{N_E} \left(\frac{dy}{d\theta} \right)_i^T \Sigma_V^{-1} \left(\frac{dy}{d\theta} \right)_i \Big|_{\theta=\hat{\theta}} \right\}^{-1} \quad (8)$$

In Equation (8), \mathbf{V}_θ^0 is the prior covariance matrix of the model parameters, which can be computed from the potential prior knowledge of parametric space. From the parameter covariance matrix, the linear confidence interval for individual parameters is computed as

$$\theta_r \in \left\{ \hat{\theta}_r \pm \sqrt{\mathbf{V}_{\theta_r}} \cdot t_{N_E \cdot N_y - N_\theta} \left(1 - \frac{\alpha}{2} \right) \right\} \quad \forall r = 1, \dots, N_\theta \quad (9)$$

In Equation (9), $t_{N_E \cdot N_y - N_\theta} \left(1 - \frac{\alpha}{2} \right)$ is the Student's t -value from a Student's t -distribution with $N_E \cdot N_y - N_\theta$ degrees of freedom and α significance level, \mathbf{V}_{θ_r} is the r -th element of covariance matrix, which denotes the variance of r -th parameter estimate. The statistical precision of parameter estimates can be analysed using the confidence intervals or from the Student's t -test. In the t -test, the test statistic computed according to Equation (10) is compared to Student's t -value from a Student's t -distribution with $N_E \cdot N_y - N_\theta$ degrees of freedom and α significance level (reference t -value)

$$t_r = \frac{\hat{\theta}_r}{\sqrt{\mathbf{V}_{\theta_r}} \cdot t_{N_E \cdot N_y - N_\theta} \left(1 - \frac{\alpha}{2} \right)} \quad \forall r = 1, \dots, N_\theta \quad (10)$$

In cases where a parameter estimate has a larger confidence interval compared to its estimated value, the t -value tends to be smaller than the reference t -value, indicating that the parameter has not been estimated precisely.

As described above, it can be inferred from both t -test and confidence interval whether the information from the dataset is sufficient to achieve a statistical precision of parameter estimates. In cases of failure of t -test, that is, if the data appears to be not informative enough, an easy method to check whether the model parameters can be precisely identified using additional data (potentially obtained through model-based design of experiments methods) is to compute the rank of the Fisher Information Matrix (FIM). In cases where the FIM is fully ranked and invertible, that is, if $\text{rank} \mathbf{H}(\hat{\theta}) = N_\theta$, it is understood that the model parameters are not perfectly correlated and have non-zero sensitivities; thereby suggesting that the parameters are practically identifiable.^[36] In situations where additional data is required to estimate the model parameters precisely, the experimental design must be recalculated to improve the identifiability of model parameters, which is not the focus of this paper. However, before attempting to design new experiments by solving an optimisation problem to improve parameter precision, it is worth studying the allocation of information across the design space based on the current data by mapping the observed information over the design space. In this work, such a mapping method was used to investigate the relative contribution of individual experiments to the observed FIM. In this mapping method, the Relative Fisher Information index (RFI)^[17b] for the adequate models was computed at each of the performed experimental conditions. The RFI index for the s -th model at conditions of the i -th experiment is obtained by the following equation

$$\text{RFI}_{is} = \frac{\mathbf{H}_i(\hat{\theta})}{\sum_{i=1}^{N_E} \mathbf{H}_i(\hat{\theta})} \quad \forall s = 1, \dots, N_m \quad (11)$$

In Equation (11), $\mathbf{H}_i(\hat{\theta})$ is the FIM of the i -th experiment and \cdot represents a metric (trace, determinant or eigenvalue) of the FIM. In this work, the trace of the FIM was used to define the RFI.

Computational resources

In the proposed framework, the solution of differential equations and simulation of kinetic models including the computation of sensitivity matrix in Equation (7) were carried out using the odeint function in SciPy package^[37] (scipy.integrate.odeint) with Isoda integrator. The parameter estimation problems were solved using the nonlinear programming (NLP) solver SLSQP. The pyDOE module in Python was used for the design of factorial and LHS experiments^[38].

Experimental procedure

The catalyst employed in this work was 5 wt.% Pd/Al₂O₃, as relatively low temperature was used in the experiments. Lower Pd loadings are common and are typically employed for higher temperature operation (≥ 600 °C). The catalyst in the microreactor was pre-treated by ramping the temperature at 10 °C min⁻¹ to 400 °C for a hold time of 30 min under the reactant mixture (3% O₂, 1.5% CH₄, 30% He and 65.5% N₂), which had been reported to enhance catalyst activity^[39], after which it was cooled to 200 °C. The pre-planned design of experiments was uploaded into the platform user interface. A stand-by condition was added as the last experimental condition, which involved ramping of temperature down to 25 °C and decreasing the reaction mixture supply to the microreactor slowly to avoid catalyst being blown away. After setting all required parameters at the user interface panel, such as specifying the file to save the measurements of composition of outlet stream, amount of catalyst, duration of each experiment, user attention was not needed until all the experiments were concluded. The lower and upper limits of the input variables for both factorial and LHS design of experiments are presented in Table 4.

A campaign consisting of eight experiments using fractional factorial design, with variables methane inlet concentration, reaction temperature, total flowrate and oxygen-methane ratio (detailed experimental conditions are given in Supporting Information, Table S1) was conducted in four replicates to gain preliminary information about the reproducibility of the automated system and characterise the measurement variance model. Subsequently, LHS experiments were used for rapid screening and selection of probable kinetic models, which took two days. On the first day the experimental platform was set-up and fifteen experiments based on LHS were performed, while the remaining fifteen experiments and the kinetic model screening were concluded on the second day. The robustness of the automated platform was also demonstrated by the LHS experiments, as the set-up operated without interruption for 10 h, obtaining 30 sample points (experimental design conditions presented in the Supporting Information,

Table 4. Experimental variable ranges used in this work.

Control variable	Lower limit	Upper limit
Temperature [°C]	250	350
Total flow rate [mL/min]	20	30
O ₂ /CH ₄ molar flowrate ratio	2	4
CH ₄ inlet mole fraction	0.015	0.025
He inlet mole fraction	0.300	0.500
O ₂ inlet mole fraction	0.030	0.100
N ₂ inlet mole fraction	0.375	0.655

Table S2). The LHS design explores large area of the design space, unlike the factorial design which is limited to only the extreme conditions (lower and upper limits) of each input. Minimum and maximum limits for each input variable were the same as for the fractional factorial experimental design. LHS based experimental conditions were generated using the PyDOE module in Python^[40]. The ‘centre’ criterion which centres the sampling points for experimental conditions within the design space was used for designing the LHS experiments. Using the ‘centre’ criterion, the LHS design had the benefit of exploring the centre of the design space which was not covered in the factorial design.

Methane catalytic combustion kinetics

Methane combustion was chosen to test the automated platform developed.



The reaction mechanism is strongly dependent on the type of catalyst used. There are four broad categories of kinetic models, which include empirical power law, Langmuir–Hinshelwood, Mars–van Krevelen and Eley–Rideal. Kinetic models from each category were selected for screening. In total thirteen kinetic rate expressions were considered as presented in Table 5.

Reparametrisation of highly correlated kinetic parameters is an important step in kinetic studies, as it enhances robustness of model identification^[13a] and minimises correlation effects among kinetic parameters^[21a]. The rate constant for the reaction is expressed as Equation (13)

$$k_i = k_{i,ref} \exp\left(\frac{-E_{ai}}{R} \left[\frac{1}{T} - \frac{1}{T_{ref}}\right]\right) \quad i = 1 \dots N_r \quad (13)$$

where k_i is the reaction rate constant ($\text{mol bar}^{-1} \text{g}^{-1} \text{s}^{-1}$), $k_{i,ref}$ is the rate constant at reference temperature, taken as the average temperature from the range of temperatures used ($\text{mol bar}^{-1} \text{g}^{-1} \text{s}^{-1}$), E_{ai} is the activation energy (J mol^{-1}), R is the ideal gas constant ($\text{J mol}^{-1} \text{K}^{-1}$), T is the reaction temperature (K), T_{ref} is the reference/mean temperature (K), $i = 1 \dots N_r$, with N_r number of reaction, for the Mars–van Krevelen model; 1, 2, and 3 refer to oxidation, reduction and product desorption steps. For Langmuir–Hinshelwood and Mars–van Krevelen models, the adsorption equilibrium constants have an analogous expression Equation (14)

$$K_i = K_{i,ref} \exp\left(\frac{-\Delta H_i}{R} \left[\frac{1}{T} - \frac{1}{T_{ref}}\right]\right) \quad i = 1 \dots N_r \quad (14)$$

where K_i is the adsorption constant (bar^{-1}), $K_{i,ref}$ is the adsorption constant at reference/mean temperature (K), ΔH is the heat of adsorption (J mol^{-1}). The Arrhenius equation in reparametrised form, which minimises correlations between parameters^[44] is given in Equation (15)

$$k_i = \exp\left(\theta_{1,i} - \frac{\theta_{2,i} 10^4}{R} \left[\frac{1}{T} - \frac{1}{T_{ref}}\right]\right) \quad (15)$$

$$\theta_{1,i} = \ln k_{i,ref} \quad \theta_{2,i} = \frac{E_{ai}}{10^4}$$

For the equilibrium adsorption constant, the reparametrised expression is Equation (16)

$$K_i = \exp\left(\theta_{3,i} - \frac{\theta_{4,i} 10^4}{R} \left[\frac{1}{T} - \frac{1}{T_{ref}}\right]\right) \quad (16)$$

$$\theta_{3,i} = \ln K_{i,ref} \quad \theta_{4,i} = \frac{\Delta H_i}{10^4}$$

Table 5. Kinetic models of methane combustion over Pd catalyst considered for screening in the automated platform.

Model	Category	Description	Rate expression	Reference
1	Empirical Power Law	Excess oxygen	$r = k p_{\text{CH}_4}$	[30a,41]
2		Weak dependence of oxygen	$r = k p_{\text{CH}_4}^{0.8}$	[42]
3			$r = k p_{\text{CH}_4}^{0.9} p_{\text{O}_2}^{0.1}$	Proposed by Hurtado <i>et al.</i> ^[27a,30b]
4			$r = k p_{\text{CH}_4}^{0.8} p_{\text{O}_2}^{0.1}$	[43]
5	Eley–Rideal	Surface reaction between adsorbed methane and molecular oxygen from gas phase	$r = \frac{k_2 K_{\text{CH}_4} p_{\text{CH}_4} p_{\text{O}_2}}{1 + K_{\text{CH}_4} p_{\text{CH}_4}}$	Proposed by Hurtado <i>et al.</i> ^[27a]
6		Surface reaction between adsorbed molecular oxygen and methane from gas phase	$r = \frac{k_2 K_{\text{O}_2} p_{\text{CH}_4} p_{\text{O}_2}}{1 + K_{\text{O}_2} p_{\text{O}_2}}$	Proposed by Hurtado <i>et al.</i> ^[27a] , Specchia <i>et al.</i> ^[31]
7		Surface reaction between adsorbed atomic oxygen and methane from gas phase	$r = \frac{k_2 p_{\text{CH}_4} \sqrt{K_{\text{O}_2} p_{\text{O}_2}}}{1 + \sqrt{K_{\text{O}_2} p_{\text{O}_2}}}$	[29]
8	Langmuir–Hinshelwood	Surface reaction between adsorbed methane and adsorbed molecular oxygen	$r = \frac{k_2 K_{\text{CH}_4} K_{\text{O}_2} p_{\text{CH}_4} p_{\text{O}_2}}{(1 + K_{\text{CH}_4} p_{\text{CH}_4} + K_{\text{O}_2} p_{\text{O}_2})^2}$	Proposed by Hurtado <i>et al.</i> ^[27a] , Specchia <i>et al.</i> ^[31]
9		Surface reaction between adsorbed methane and dissociatively adsorbed oxygen	$r = \frac{k K_{\text{CH}_4} p_{\text{CH}_4} \sqrt{K_{\text{O}_2} p_{\text{O}_2}}}{(1 + K_{\text{CH}_4} p_{\text{CH}_4} + \sqrt{K_{\text{O}_2} p_{\text{O}_2}})^2}$	Proposed by Hurtado <i>et al.</i> ^[27a] , Specchia <i>et al.</i> ^[31]
10		Surface reaction between adsorbed methane and two atomic adsorbed oxygens	$r = \frac{k K_{\text{CH}_4} p_{\text{CH}_4} K_{\text{O}_2} p_{\text{O}_2}}{(1 + K_{\text{CH}_4} p_{\text{CH}_4} + \sqrt{K_{\text{O}_2} p_{\text{O}_2}})^3}$	Proposed by Hurtado <i>et al.</i> ^[27a] , Specchia <i>et al.</i> ^[31]
11	Mars–van Krevelen	Negligible chemisorbed oxygen and fast desorption of products	$r = \frac{k_1 k_2 p_{\text{CH}_4} p_{\text{O}_2}}{k_1 p_{\text{O}_2} + 2k_2 p_{\text{O}_2}}$	Proposed by Hurtado <i>et al.</i> ^[27a]
12		Slow desorption of reaction products	$r = \frac{k_1 k_2 p_{\text{CH}_4} p_{\text{O}_2}}{k_1 p_{\text{O}_2} + 2k_2 p_{\text{O}_2} + (k_1 k_2 / k_3) p_{\text{CH}_4} p_{\text{O}_2}}$	[27a] proposed by Specchia <i>et al.</i> ^[31]
13		Methane weakly adsorbed on the catalyst surface	$r = \frac{k_1 k_2 K_{\text{CH}_4} p_{\text{CH}_4} p_{\text{O}_2}}{k_1 p_{\text{O}_2} + 2k_2 K_{\text{CH}_4} p_{\text{CH}_4}}$	Proposed by Hurtado <i>et al.</i> ^[27a]

When only a reference is provided, it indicates that the model was used by the authors, while “Proposed by” indicates that the model was considered as one of potential candidate models.

Reactor model

The Mears criterion was used to check for external mass transfer limitations (see Supporting Information, section 2.1). A value of 0.026 was obtained, hence external mass transfer resistance was ignored. The Weisz–Prater criterion was evaluated to check for internal mass transfer limitations (see Supporting Information, section 2.2). A value of 0.13, was calculated, hence internal mass transfer resistances were assumed negligible. For external heat transfer limitation to be ignored the computed value from the Mear's criterion should be < 0.15 , but a value of 0.3 was obtained, hence the temperature difference between the fluid and catalyst surface was computed (see Supporting Information, section 3.1) and for the kinetic studies this temperature difference was added to the measured temperature to approximate the catalyst particle temperature. Internal heat transfer resistance could be ignored based on the computed value of 0.007 for the Anderson criterion (see Supporting Information, section 3.2). The reactor was assumed to behave as an ideal plug flow reactor (PFR) (see Supporting Information, section 4.0)^[45]. The aspect ratio (microreactor depth (420 μm) over catalyst particle average size (69 μm)) was 6.1. An aspect ratio value > 10 is typically required to minimise the negative impact of wall effects. Though less than this threshold, a similar value has been acceptable for similar small catalyst size, since fast diffusion at this scale can minimise wall effects^[46]. As shown in 2.1, the reactor showed a constant temperature profile. Considering all the above, a pseudo-homogeneous isothermal PFR model was used for the calculations Equation (17)

$$\frac{dy_i}{dw} = \frac{RT}{vP_{avg}} s_i r_i \quad i = \text{CH}_4, \text{O}_2, \text{CO}_2, \text{H}_2\text{O} \quad (17)$$

where s_i is the stoichiometric coefficient for the i -th species, r_i is the rate of reaction, v is the volumetric flow rate, y is the mole fraction, P_{avg} is the average reactor pressure.

Acknowledgements

S.G.B. gratefully acknowledges support by the Petroleum Technology Development Fund for his studentship. We thank Johnson Matthey for providing the catalyst used.

Conflict of Interest

The authors declare no conflict of interest.

Data Availability Statement

The data that support the findings of this study are available in the supplementary material of this article.

Keywords: automation · kinetics · methane · micropacked-bed · palladium.

- [1] a) K. F. Jensen, *AIChE J.* **2017**, *63*, 858–869; b) N. Al-Rifai, E. Cao, V. Dua, A. Gavriilidis, *Curr. Opin. Chem. Eng.* **2013**, *2*, 338–345.
[2] K. F. Jensen, B. J. Reizman, S. G. Newman, *Lab Chip* **2014**, *14*, 3206–3212.

- [3] D. C. Fabry, E. Sugiono, M. Rueping, *React. Chem. Eng.* **2016**, *1*, 129–133.
[4] a) E. Cao, G. Brett, P. J. Miedziak, J. M. Douthwaite, S. Barrass, P. F. McMillan, G. J. Hutchings, A. Gavriilidis, *Catal. Today* **2017**, *283*, 195–201; b) B. A. Rizkin, F. G. Popovic, R. L. Hartman, *J. Vac. Sci. Technol. A* **2019**, *37*, 1–22; c) B. J. Reizman, K. F. Jensen, *Org. Process Res. Dev.* **2012**, *16*, 1770–1782.
[5] J. Yue, F. H. Falke, J. C. Schouten, T. A. Nijhuis, *Lab Chip* **2013**, *13*, 4855–4863.
[6] a) R. Schalk, D. Geogerg, J. Staubach, M. Raedle, F. J. Methner, T. Beuermann, *J. Biosci. Bioeng.* **2017**, *123*, 651–657; b) J. S. Moore, K. F. Jensen, *Angew. Chem. Int. Ed. Engl.* **2014**, *53*, 470–473; c) K. C. Aroh, K. F. Jensen, *React. Chem. Eng.* **2018**, *3*, 94–101; d) J. Keybl, K. F. Jensen, *Ind. Eng. Chem. Res.* **2011**, *50*, 11013–11022.
[7] a) G. Rinke, A. Ewinger, S. Kerschbaum, M. Rinke, *Microfluid. Nanofluid.* **2010**, *10*, 145–153; b) E. Cao, S. Firth, P. F. McMillan, A. Gavriilidis, *Catal. Today* **2007**, *126*, 119–126.
[8] a) J. P. McMullen, K. F. Jensen, *Org. Process Res. Dev.* **2010**, *14*, 1169–1176; b) J. P. McMullen, K. F. Jensen, *Org. Process Res. Dev.* **2011**, *15*, 398–407; c) A.-C. Bédard, A. Adamo, K. C. Aroh, M. G. Russell, A. A. Bedermann, J. Torosian, B. Yue, K. F. Jensen, T. F. Jamison, *Science* **2018**, *361*, 1220–1225; d) C. Waldron, A. Pankajakshan, M. Quaglio, E. Cao, F. Galvanin, A. Gavriilidis, *React. Chem. Eng.* **2019**, *4*, 1623–1636.
[9] a) A. Echtermeyer, Y. Amar, J. Zakrzewski, A. Lapkin, Beilstein *J. Org. Chem.* **2017**, *13*, 150–163; b) N. Cherkasov, Y. Bai, A. J. Expósito, E. V. Rebrov, *React. Chem. Eng.* **2018**, *3*, 769–780.
[10] a) M. N. Kashid, A. Renken, L. Kiwi-Minsker, *Chem. Eng. Sci.* **2011**, *66*, 3876–3897; b) Y. Voloshin, A. Lawal, *Chem. Eng. Sci.* **2010**, *65*, 1028–1036; c) D. Russo, *Appl. Sci.* **2021**, *11*, 1042–1061; d) M. L. Satuf, J. Macagno, A. Manassero, G. Bernal, P. A. Kler, C. L. A. Berli, *Appl. Catal. B* **2019**, *241*, 8–17.
[11] A. A. Volk, M. Abolhasani, *Trends Chem.* **2021**, *3*, 519–522.
[12] a) R. Goodell, J. P. McMullen, N. Zaborenko, J. R. Maloney, C. X. Ho, K. F. Jensen, J. A. Porco, Jr., A. B. Beeler, *J. Org. Chem.* **2009**, *74*, 6169–6180; b) J. Reizman, K. F. Jensen, *Acc. Chem. Res.* **2016**, *49*, 1786–1796; c) M. Rubens, J. V. Herck, T. Junkers, *ACS Macro Lett.* **2019**, *8*, 1437–1441; d) L. Hall, C. J. Taylor, R. Labes, A. F. Massey, R. Menzel, R. A. Bourne, T. W. Chamberlain, *Chem. Commun.* **2021**, *57*, 4926–4929; e) A. D. Clayton, A. M. Schweidtmann, G. Clemens, J. A. Manson, C. J. Taylor, C. G. Niño, T. W. Chamberlain, N. Kapur, A. J. Blacker, A. A. Lapkin, R. A. Bourne, *Chem. Eng. J.* **2020**, *384*, 123340; f) D. Perera, J. W. Tucker, S. Brahmabhatt, C. J. Helal, A. Chong, W. Farrell, P. Richardson, N. W. Sach, *Science* **2018**, *359*, 429–434.
[13] a) M. Quaglio, C. Waldron, A. Pankajakshan, E. Cao, A. Gavriilidis, E. S. Fraga, F. Galvanin, *Chem. Ing. Tech.* **2019**, *91*, 268–276; b) C. Waldron, A. Pankajakshan, M. Quaglio, E. Cao, F. Galvanin, A. Gavriilidis, *Ind. Eng. Chem. Res.* **2019**, *58*, 22165–22177; c) C. J. Taylor, M. Booth, J. A. Manson, M. J. Willis, G. Clemens, B. A. Taylor, T. W. Chamberlain, R. A. Bourne, *Chem. Eng. J.* **2021**, *413*, 127017; d) C. Waldron, A. Pankajakshan, M. Quaglio, E. Cao, F. Galvanin, A. Gavriilidis, *React. Chem. Eng.* **2020**, *5*, 112–123.
[14] G. Franceschini, S. Macchietto, *Chem. Eng. Sci.* **2008**, *63*, 4846–4872.
[15] S. Vajda, H. Rabitz, E. Walter, Y. Lecourtier, *Chem. Eng. Commun.* **1989**, *83*, 191–219.
[16] A. Gábor, A. F. Villaverde, J. R. Banga, *BMC Syst. Biol.* **2017**, *11*, 54–69.
[17] a) S. P. Asprey, S. Macchietto, *Comput. Chem. Eng.* **2000**, *24*, 1261–1267; b) F. Galvanin, E. Cao, N. Al-Rifai, A. Gavriilidis, V. Dua, *Comp. Chem. Eng.* **2016**, *95*, 202–215.
[18] P. Gélin, M. Primet, *Appl. Catal. B* **2002**, *39*, 1–37.
[19] P. Araya, S. Guerrero, J. Robertson, F. J. Gracia, *Appl. Catal. A* **2005**, *283*, 225–233.
[20] a) M. Lyubovskiy, L. Pfefferle, *Appl. Catal. A* **1998**, *173*, 107–119; b) A. Machocki, M. Rotko, B. Stasinska, *Catal. Today* **2008**, *137*, 312–317; c) F. H. Ribeiro, M. Chow, R. A. D. Betta, *J. Catal.* **1994**, *146*, 537–544; d) A. K. Datye, J. Bravo, T. R. Nelson, P. Atanasova, M. Lyubovskiy, L. Pfefferle, *Appl. Catal. A* **2000**, *198*, 179–196.
[21] a) G. Groppi, *Catal. Today* **2003**, *77*, 335–346; b) D. Ciuparu, N. Katsikis, L. Pfefferle, *Appl. Catal. A* **2001**, *216*, 209–215; c) K.-i. Fujimoto, F. H. Ribeiro, M. Avalos-Borja, E. Iglesia, *J. Catal.* **1998**, *179*, 431–442.
[22] D. Ciuparu, L. Pfefferle, *Appl. Catal. A* **2001**, *218*, 197–209.
[23] a) D. Ciuparu, M. R. Lyubovskiy, E. Altman, L. D. Pfefferle, A. Datye, *Catal. Rev.* **2002**, *44*, 593–649; b) S. H. Oh, P. J. Mitchell, R. M. Siewert, *J. Catal.* **1991**, *132*, 287–301; c) R. Burch, P. K. Loader, *Appl. Catal. B* **1994**, *5*, 149–164; d) Y.-H. C. Chin, C. Buda, M. Neurock, E. Iglesia, *J. Am. Chem. Soc.* **2013**, *135*, 15425–15442; e) X. Zou, Z. Rui, S. Song, H. Ji, *J. Catal.* **2016**,

- 338, 192–201; f) H. Duan, R. You, S. Xu, Z. Li, K. Qian, T. Cao, W. Huang, X. Bao, *Angew. Chem. Int. Ed. Engl.* **2019**, *58*, 12043–12048.
- [24] a) A. Hellman, A. Resta, N. M. Martin, J. Gustafson, A. Trincherro, P. A. Carlsson, O. Balmes, R. Felici, R. van Rijn, J. W. Frenken, J. N. Andersen, E. Lundgren, H. Gronbeck, *J. Phys. Chem. Lett.* **2012**, *3*, 678–682; b) J. Nilsson, P.-A. Carlsson, S. Fouladvand, N. M. Martin, J. Gustafson, M. A. Newton, E. Lundgren, H. Grönbeck, M. Skoglundh, *ACS Catal.* **2015**, *5*, 2481–2489.
- [25] a) J. J. Willis, A. Gallo, D. Sokaras, H. Aljama, S. H. Nowak, E. D. Goodman, L. Wu, C. J. Tassone, T. F. Jaramillo, F. Abild-Pedersen, M. Cargnello, *ACS Catal.* **2017**, *7*, 7810–7821; b) R. F. Hicks, H. Qi, M. L. Young, R. G. Lee, *J. Catal.* **1990**, *122*, 295.
- [26] a) D. Wang, J. Gong, J. Luo, J. Li, K. Kamasamudram, N. Currier, A. Yezerets, *Appl. Catal. A* **2019**, *572*, 44–50; b) G. Zhu, J. Han, D. Y. Zemlyanov, F. Ribeiro, *J. Phys. Chem. B* **2005**, *109*, 2331–2337.
- [27] a) P. Hurtado, S. Ordóñez, H. Sastre, F. V. Diez, *Appl. Catal. B* **2004**, *51*, 229–238; b) H. Stotz, L. Maier, A. Boubnov, A. T. Gremminger, J. D. Grunwaldt, O. Deutschmann, *J. Catal.* **2019**, *370*, 152–175.
- [28] a) J. Xu, L. Ouyang, W. Mao, X.-J. Yang, X.-C. Xu, J.-J. Su, T.-Z. Zhuang, H. Li, Y.-F. Han, *ACS Catal.* **2012**, *2*, 261–269; b) R. Kikuchi, S. Maeda, K. Sasaki, S. Wennerstrom, K. Eguchi, *Appl. Catal. A* **2002**, *232*, 23–28; c) L. Ma, D. L. Trimm, C. Jiang, *Appl. Catal. A* **1996**, *138*, 275–283.
- [29] S. Seimanides, M. Stoukides, *J. Catal.* **1986**, *98*, 540–549.
- [30] a) M. Aryafar, F. Zaera, *Catal. Lett.* **1997**, *48*, 173–183; b) J. C. van Geiesen, F. R. van den Berg, J. L. Kleinen, A. J. van Dillen, J. W. Geus, *Catal. Today* **1999**, *47*, 287–293.
- [31] S. Specchia, F. Conti, V. Specchia, *Ind. Eng. Chem. Res.* **2010**, *49*, 11101–11111.
- [32] J. F. Weaver, C. Hakanoglu, J. M. Hawkins, A. Asthagiri, *J. Chem. Phys.* **2010**, *132*, 024709–024719.
- [33] I. Kim, M. J. Liebman, T. F. Edgar, *AIChE J.* **1990**, *36*, 985–993.
- [34] P. R. Killeen, *Psychol. Sci.* **2005**, *16*, 345–353.
- [35] H. E. Reinhardt, *SIAM Rev.* **1975**, *17*, 703–704.
- [36] T. J. Rothenberg, *Econometrica* **1971**, *39*, 577–591.
- [37] P. Virtanen, R. Gommers, T. E. Oliphant, M. Haberland, T. Reddy, D. Cournapeau, E. Burovski, P. Peterson, W. Weckesser, J. Bright, S. J. v. d. Walt, M. Brett, J. Wilson, K. J. Millman, N. Mayorov, A. R. J. Nelson, E. Jones, R. Kern, E. Larson, C. J. Carey, Í. Polat, Y. Feng, E. W. Moore, J. VanderPlas, D. Laxalde, J. Perktold, R. Cimrman, I. Henriksen, E. A. Quintero, C. R. Harris, A. M. Archibald, A. H. Ribeiro, F. Pedregosa, P. v. Mulbregt, S. Contributors, *Nat. Methods* **2020**, *17*, 261–272.
- [38] D. Montgomery, *Design and analysis of experiments*, John Wiley & Sons, Hoboken, New Jersey, **2013**.
- [39] J. H. Lee, D. L. Trimm, *Fuel Process. Technol.* **1995**, *42*, 339–359.
- [40] “pyDOE: The experimental design package for python,” <https://pythonhosted.org/pyDOE/>.
- [41] Y. Xin, S. Lieb, H. Wang, C. K. Law, *J. Phys. Chem. C* **2013**, *117*, 19499–19507.
- [42] C. F. Cullis, D. L. Trimm, *J. Chem. Soc. Faraday Trans.* **1972**, *1*, 1406–1412.
- [43] Y.-F. Y. Yao, *Ind. Eng. Chem. Prod. Res. Dev.* **1980**, *19*, 293–298.
- [44] G. Buzzi-Ferraris, F. Manenti, *Chem. Eng. Sci.* **2009**, *64*, 1061–1074.
- [45] F. Kapteijn, J. A. Moulijn, “Laboratory Catalytic Reactors: Aspects of Catalyst Testing” Chapter 9 in *Handbook of Heterogeneous Catalysis*, Vol. 1, 2nd ed., Wiley-VCH, Weinheim, **2008**.
- [46] S. K. Ajmera, M. W. Losey, K. F. Jensen, *AIChE J.* **2001**, *47*, 1639–1647.

Manuscript received: July 30, 2022

Version of record online: November 11, 2022